Medical Engineering and Physics 37 (2015) 979–986

Contents lists available at ScienceDirect

Medical Engineering and Physics

journal homepage: www.elsevier.com/locate/medengphy

Automatic detection of selective arterial devices for advanced visualization during abdominal aortic aneurysm endovascular repair

Simon Lessard[a,d], Claude Kauffmann[a,d], Marcus Pfister[f], Guy Cloutier[b,d], Éric Thérasse[e], Jacques A. de Guise[c,d], Gilles Soulez[a,d,e,*]

[a] Laboratoire clinique du traitement de l'image (LCTI), Canada
[b] Laboratoire de biorhéologie et d'ultrasonographie médicale (LBUM), Canada
[c] Laboratoire de recherche en imagerie et orthopédie (LIO), Canada
[d] Centre de recherche du centre hospitalier de l'Université de Montréal (CRCHUM), Canada
[e] Department of Radiology, Centre hospitalier de l'Université de Montréal (CHUM), Canada
[f] Siemens AG, Healthcare Sector, Forchheim, Germany

ARTICLE INFO

Article history:
Received 8 December 2014
Revised 6 July 2015
Accepted 22 July 2015

Keywords:
Gradient norm shift
Radiopaque marker
Automatic segmentation
Endovascular devices
Interventional radiology

ABSTRACT

Here we address the automatic segmentation of endovascular devices used in the endovascular repair (EVAR) of abdominal aortic aneurysms (AAA) that deform vascular tissues. Using this approach, the vascular structure is automatically reshaped solving the issue of misregistration observed on 2D/3D image fusion for EVAR guidance. The endovascular devices we considered are the graduated pigtail catheter (PC) used for contrast injection and the stent-graft delivery device (DD). The segmentation of the DD was enhanced using an asymmetric Frangi filter. The segmented geometries were then analysed using their specific features to remove artefacts. The radiopaque markers of the PC were enhanced using a fusion of Hessian and newly introduced gradient norm shift filters. Extensive experiments were performed using a database of images taken during 28 AAA-EVAR interventions. This dataset was divided into two parts: the first half was used to optimize parameters and the second to compile performances using optimal values obtained. The radiopaque markers of the PC were detected with a sensitivity of 88.3% and a positive predictive value (PPV) of 96%. The PC can therefore be positioned with a majority of its markers localized while the artefacts were all located inside the vessel lumen. The major parts of the DD, the dilatator tip and the pusher surfaces, were detected accurately with a sensitivity of 85.9% and a PPV of 88.7%. The less visible part of the DD, the stent enclosed within the sheath, was segmented with a sensitivity of 63.4% because the radiopacity of this region is low and uneven. The centreline of the DD in this stent region was alternatively traced within a 0.74 mm mean error. The automatic segmentation of endovascular devices during EVAR is feasible and accurate; it could be useful to perform elastic registration of the vascular lumen during endovascular repair.

1. Introduction

Surgical repair of the aneurysmal segment remains the gold-standard treatment of abdominal aortic aneurysm (AAA). However, postoperative mortality rises from 4.6% [1] to approximately 10% [2] when the patient suffers from severe comorbidity. The alternative is an interventional procedure consisting of endovascular repair (EVAR) with stent graft (SG) [3]. Lower perioperative mortality and morbidity rates have been reported for EVAR, even though the durability of aneurysm exclusion is compromised by frequent endoleaks that prolong the intervention or require re-intervention. The endovascular intervention is guided by digital subtraction angiography (DSA) and fluoroscopy in order to properly deliver the SG and seal of the aneurysm while avoiding coverage of side branches such as renal or internal iliac arteries. This meticulous delivery requires skill to position the C-arm to account for parallax compensation. Since vessels are not visible under fluoroscopy, vascular opacification with iodinated contrast agent is required. Contrast-induced nephropathy is, however, a concern in this population with a high prevalence of renal failure [4]. Moreover, the recently introduced fenestrated SG [5] requires precise vascular mapping to position and align the fenestrations of the SG with targeted vascular branches (renal or digestive arteries) of the aorta.

* Corresponding author at: Centre de recherche du centre hospitalier de l'Université de Montréal (CRCHUM), Canada.
E-mail address: gilles.soulez.chum@ssss.gouv.qc.ca (G. Soulez).

http://dx.doi.org/10.1016/j.medengphy.2015.07.007
1350-4533/

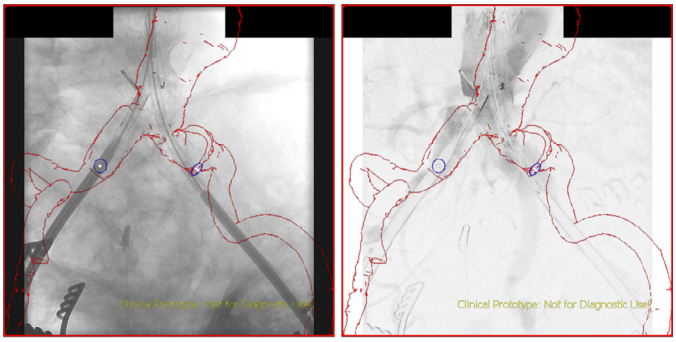

(a) Fluoroscopy (b) DSA

Fig. 1. Vascular deformation observed during endovascular repair. The lumen on the pre-operative CT is outlined in red and the ostium are tagged in blue. (For interpretation of the references to colour in this figure legend, the reader is referred to the web version of this article.)

1.1. Related work

Improving the fluoroscopic guidance during the EVAR procedure is the subject of intense research effort. Some software solutions are already available such as fusion of the preoperative multidetector contrast CT (MDCT) used for intervention planning with live fluoroscopy. The vascular structure extracted from the MDCT can be segmented [6–9] or simply accentuated[10]. This volumetric information is then registered on live fluoroscopic images, either directly on the 2D image (2D-3D registration) [8,10,11] or with a perioperative cone-beam CT acquisition (3D-3D registration) [7]. Misregistrations have been observed during these guided interventions interventions [6,7,11–14]. They are caused mainly by patient motion and postural changes, as well as by the rigidity of endovascular devices inducing deformation of vascular structures. As seen in Fig. 1, the aorta path is shifted and the iliac arteries are heavily deformed. These distortions constitute a major flaw and as a consequence, physicians are reluctant to rely solely on a numerical vascular overlay. In order to overcome the positional drift associated with patient motion, tracking of anatomical landmarks such as the bones can be used. However, the vascular deformation induced by stiff endovascular devices can only be corrected by shape reforming. Using finite element analysis, Kaladji et al. [8] proposed a mechanical model of the vascular structure by submitting the structure to a stiff guidewire in order to estimate the deformation prior to the intervention. This new model was then compared to the live fluoroscopic image at the proper sequence with the guidewire in place. Once registered, the centreline mean error was 2.3 mm. The major drawback of this approach is having a priori knowledge of the type and number of devices to be used and their exact positions. In practise, the interventional radiologist can use different guidewires and catheters at different locations, depending on the progression of the catheterization/intervention process making prior calculation of the different procedural steps very cumbersome.

Segmentation strategies of endovascular devices have been studied for many years beginning with the segmentation of guidewires [15–24] and catheters [25–29], followed by deployed stents [30–32]. More recent works show promising performance that relies on anisotropic filtering combined with active contour segmentation or probabilistic line segment reconstruction. Radiopaque markers are frequently inserted in catheters to improve their detection under fluoroscopy. Detection of these radiopaque markers has frequently been used for oncology radiation targeting [33–38]. Classical pattern matching techniques are the most popular segmentation approaches proposed along with intensity correlation matching: a method that relies entirely on distinctive metrics [39]. Since fiducial markers are quite visible and have distinctive features, no marker enhancement filtering technique has yet been reported.

1.2. Contribution

Here, we propose a real-time deformable vascular model that uses the current position of endovascular devices as determined by live fluoroscopic images. This simple model could potentially improve the vascular overlay and reduce the need for contrast agent. The proposed model is deformed by the live position of endovascular devices, therefore an automatic (and real-time) identification and segmentation is mandatory.

This paper presents an algorithm workflow to automatically segment relevant endovascular devices used during AAA EVAR. The two major arterial devices considered are the pigtail catheter (PC) and the stent delivery device (DD). In these arteries, There segmentation is a milestone to enables elastic deformation of vascular structures and to eventually improve the accuracy of 2D/3D registration. There are no reports on endovascular tools that have unique imaging characteristics that have not yet been segmented. In addition, the filtering enhancement of endovascular tools on live fluoroscopy is often neglected as is the case for the radiopaque markers and while of interest, no filtering strategies have been reported.

The materials and methods present, at first, the analysis of enhancement filtering. An original filtering technique is detailed and compared with similar and known strategies. The actual segmentation that follows is tested offline on a large dataset of images taken during EVAR interventions.

2. Materials and methods

Typically, the EVAR procedure starts with the insertion of stiff guidewire that initiates the deformation of the vascular structure. This follows a 5-French PC in the abdominal aorta through the contralateral iliac artery prior to the insertion of the DDs (main and contralateral). This PC enables serial contrast injection to guide SG delivery at different steps of the procedure for digital subtraction angiography. The radiopaque (graduated) markers are evenly spaced and are used for measurement and alignment on live fluoroscopy. Afterwards, the main body DD- a 16- to 22-French sheath, including the folded main body SG component, is advanced over a stiff guidewire through the ipsilateral femoral artery. Finally, after cannulation of the contralateral limb of the main body through the contralateral femoral artery, a contralateral DD (between 12- and 18- French) is advanced over a stiff guidewire to complete the AAA exclusion and to maintain the perfusion of the ipsilateral leg. The stiff guidewire and the DDs are known to deform the vascular structure [12] (Fig. 1). The PC and the DDs are the endovascular devices that must be segmented automatically in order to perform an automatic deformation of the vascular structure.

2.1. Segmentation of the pigtail catheter

The segmentation in image analysis is usually achieved by a 3-step procedure. First, the original image is filtered to enhance the geometrical aspects of the object of interest while blurring the rest of the image. Second, the object of interest is then segmented using various methods based on adaptive thresholds, shape and optimization schemes. Lastly, the data is analysed for concordance to specific features. The method proposed here for the segmentation of the radiopaque marker of the PC follows this classical approach.

2.1.1. Existing filters

Although effective, filtering techniques in radiopaque segmentation have not been reported but the enhancement of blob-like structures has been more documented. Hence, small structures are highly responsive to the second derivative. Our first candidate is the classical Laplacian of Gaussian (LoG), combining the derivative with smoothing [40]. The second candidate, the Hessian matrix, is more

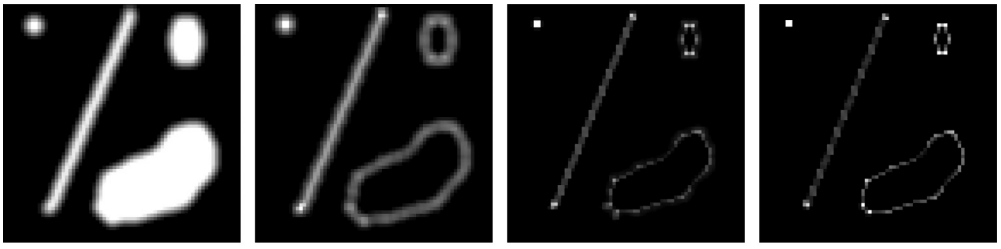

(a) Synthetic image (b) $\mathbf{I}_{GNS-1}$ (c) $\mathbf{I}_{GNS-2}$ (d) $\mathbf{I}_{GNS-3}$

Fig. 2. Gradient norm shift example.

meaningful when decomposed in eigenvalues whereby the first eigenvalue denotes a stable linear object as it emphasizes a strong second derivative with a large x and y difference. As a complement, a high value of the second eigenvalue denotes a strong second derivative with minimal x and y difference. Thus, a circular structure would have such a local maxima and symmetric x and y behaviour. In addition, when combined with Gaussian smoothing, the second Hessian eigenvalue is a straightforward filter [41].

2.1.2. Gradient norm shift

The first derivative, the gradient, has been commonly used in active contouring as an external force. The gradient field is redistributed around strong values to expand its reach; this popular algorithm is the gradient vector flow [42]. However, for small objects like radiopaque markers, the active contour is not appropriate. To address this, we propose a novel approach that favours small closed contour objects over other geometries in order to compute an effective small circle enhancement filter. The first image derivative (the gradient) is also effective in locating sharp image features, but it has to be interpreted distinctively. A radiopaque marker has a circular shape, thus all edge gradient vectors tend to point towards the contour or outwards, depending on its contrast with the background. Hence, closed objects have more centre-pointing vectors than open objects. If a closed object is regular and small, the alignment of centre-pointing vectors can serve as an enhancement factor. With more vectors pointing toward a common centre, a flow-sum algorithm will enhance more circular structures than lines.

This newly proposed filter is a shifting operation of the gradient norm towards the gradient direction and is referred to as the Gradient Norm Shift (GNS). A pre-Gaussian filter is also applied as the second derivative approaches.

A filtered image $\mathbf{I}_{GNS}$ is computed by shifting the gradient norm one unit in the gradient direction:

$$I_{GNS}(x + u_x(x,y), y + u_y(x,y)) = |\bigtriangledown I_\sigma(x,y)|, \quad \forall x = 1 \ldots m, y = 1 \ldots n \tag{1}$$

where m and n are the image size, u_x and u_y the gradient unit vector direction and $|\bigtriangledown I_\sigma|$ the gradient norm. I_σ is the Gaussian smooth input image. This operation can be repeated using the original direction unit vector until the contributing gradient norm has reached its respective summit, and is dependent on the closed contour size. The number of iterations (unit shifts) is indicated as a subscript, as in $\mathbf{I}_{GNS-3}$ as a 3-iteration shift. Fig. 2 is an example of the filter applied on a synthetic image. The upper-left structure of interest is thinner and gains in intensity as the iteration shifts increase.

2.1.3. Segmentation

A simpler method to segment an object in an image is by using the threshold. The threshold level can be fixed over a filtered image, adapted to the histogram distribution, or progressively adapted using the hysteresis feature. The histogram-evaluated threshold is useful when the object of interest is of regular grey level intensity and occupies a large area in the image such that it is significantly visible in the histogram. The hysteresis threshold and similar adaptive techniques are useful for region growing-like algorithms, again, with objects of significant size. For the segmentation of very small objects, the simple threshold is the logical approach.

By definition, an ideal filter would produce the best enhancement over a wide variety of images. In order to determine and adjust this filter, an extensive numerical experiment must be performed on a large image database. Classically, measuring the performance of a filter is determined by the signal to noise ratio (SNR). To determine the best performance of a filter, the SNR is calculated repeatedly with multiple parameters on the same images, representing all possible combinations of those parameters. The highest ratios indicate the best performance of each filter.

2.1.4. Data analysis

The analysis of the segmented data allows the recognition of the true positives over false positives. The false positives correspond to artefacts in the image-processing study. They appear everywhere when an image feature mimics a marker to be detected. In order to reduce artefacts to a minimum, an analysis can be performed by knowing the particular features of the PC radiopaque marker.

The PC markers are evenly spaced at every centimetre along the catheter's length. Thus, the pixel size at the object level seen on screen can be estimated offline using the parameters available in the DICOM header:

$$Pixel\ Size = \frac{Imager\ Pixel\ Spacing * Distance\ Source\ Patient}{Distance\ Source\ Detector} \tag{2}$$

$$Estimated\ Marker\ Distance = \frac{10\text{mm}}{Pixel\ Size}(\text{pixel}) \tag{3}$$

The computer program provides the algorithm with the pixel size. The actual length observed between two markers in a projected view can be off this estimate because the C-arm detector panel may not be parallel to the entire catheter course, as shown in Fig. 3. The C-arm position is usually determined to show both renal artery ostia in order to release the SG without covering renal arteries. Thus, this position is in most cases a top view with a slight left anterior oblique angulation with rare craniocaudal rotation. Anterior oblique angulation does not compromise the parallelism between the catheter course and the detector panel, but major craniocaudal rotation (needed for complex EVAR cases) from the top view can induce a reduction in the marker distances. Also, the catheter or a portion of it may be higher or lower than the C-arm patient origin. It is a 3D geometry in a conic projection beam, thus a variation in the table height position can induce a variation in the size projected in either direction. An acceptance interval on the estimated marker distance helps manage these length modifications.

A second selective feature is the repetition of markers in a chained sequence. Thus, a chain is constructed with an assemblage of markers

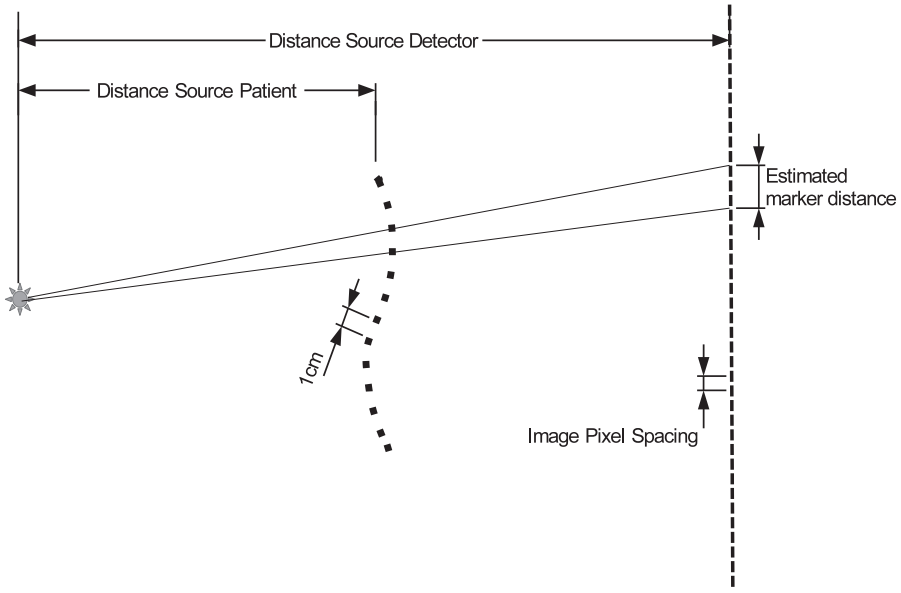

Fig. 3. Pigtail marker projection.

with acceptable distances as well as a coherent line segment angular variation.

2.2. Segmentation of the delivery device

Like the radiopaque marker, the segmentation of the DD is also a straightforward filtering scheme of segmentation and analysis. The typical usage of such devices helps the proper tuning of these three steps. The DD is pushed from the femoral artery into the abdominal aorta. The typical C-arm position discussed in Section 2.1.4 produces an image in which the DD is display as a curved path from bottom to top.

2.2.1. Filter

The enhancement of line-like structures in a medical image is commonly performed with the Frangi et al. filter [43], based on the eigenvalues of the Hessian matrix. The Frangi filter is designed to enhance contrasted vascular structure and it has also been used for guidewire detection [18,22]. For the enhancement of the DD, the width varies from one image to another. The Gaussian standard deviation σ can be adjusted to optimally respond to a specific pixel size. Also, the σ for the vertical image derivative component is set higher than the horizontal component in order to more efficiently enhance vertical line-like structures, as it is expected that the device will appear from the bottom to the top of the image.

2.2.2. Segmentation

In the image, the area occupied by the device area is more significant than the radiopaque marker thus, propitious to histogram-adaptive algorithm. The Otsu [44] method for separating image features based on the minimization of intra-class variances is a robust and effective solution to the segmentation of the DD.

2.2.3. Analysis

In the third step, the analysis utilizes a priori knowledge of the setup as well as the image registered pre-operatively. The latter is retraced using a path-tracking method.

A priori knowledge. With some knowledge of the DD location, an analysis can be computed to potentially remove false-positive objects. In the present prototype software, the pre-interventional vascular meshes are initially registered with the peri-interventional C-arm CT (Fig. 4a). As the intervention progresses, the movements of

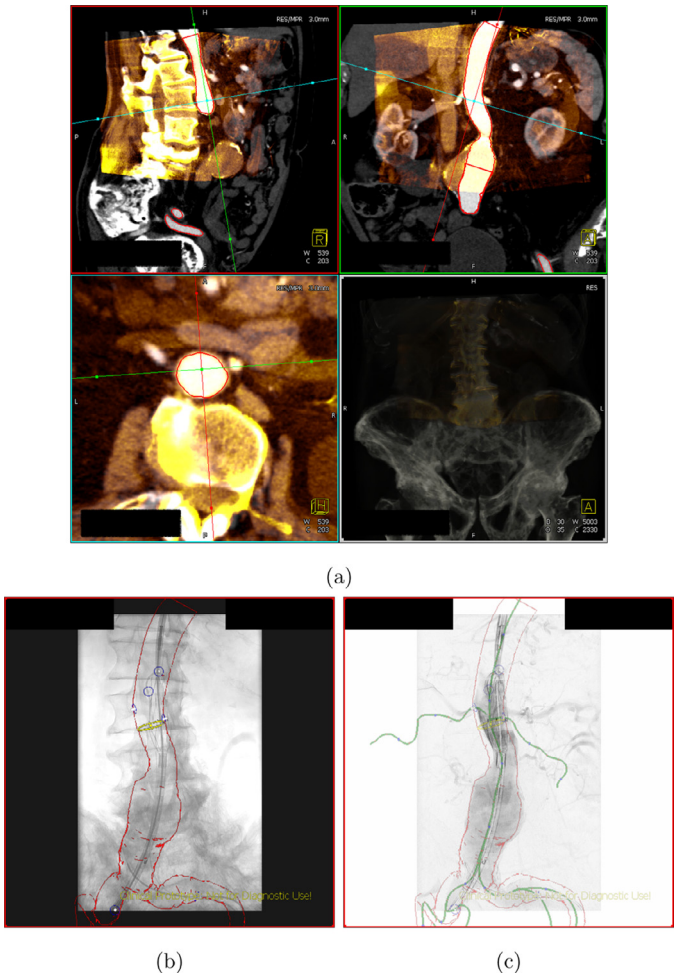

(a) (b) (c)

Fig. 4. Prototype software registration, (a) pre-operative CT and peri-operative C-arm CT vascular registration (3 planar views and a 3D maximum intensity projection), (b) 2D fluoroscopy registration showing the diamond shape and the delivery device, (c) corresponding 2D angiography showing a lateral shift of the lumen due to the rigidity of the delivery device.

the patient can be corrected by a manual registration based on a DSA, as seen on Fig. 4c and reported in [13]. On the live fluoroscopy display, the segmented lumen is outlined in red, the ostium tagged in blue, and a yellow circle shows the upper limits for the graft to avoid covering the lower renal artery (Fig. 4b). The centrelines are then projected onto the live image, as seen in green in Fig. 4c. It is obvious that the DD will go from one iliac artery to the abdominal aorta. By registering the projection of centrelines on the image, they can be used for tracking restrictive regions and for entry points at the bottom of the image, as well as for exit points at the top. Even though the vascular structure is expected to be deformed, by establishing some maximum deformation amplitudes, restrictive regions of interest can be applied. This strategy can potentially remove artefacts and false vascular pathways.

2.2.4. Path tracking

The region of interest around the pre-operative centrelines can be improved by tracking the highest and continuous path from bottom to top in the filtered image (Fig. 7b). This path leads most likely to the centreline of the DD. Thus, selecting only the digital object along this path ensures the removal of potential artefacts outside the course of the device. The path tracking in an image consists of a cumulative cost calculation in pixel proximity moving through the rows from bottom to top. The minimal (or maximal) cost cumulated at the top of the image indicates the most promising continuous and high responsive path in the image. With knowledge of the centreline projection, if the iliac bifurcation appears in the image, the path tracking algorithm is computed twice to track both iliac arteries present in the image.

2.3. Experiments

A database of images from EVAR procedures was gathered with the authorization of the Centre Hospitalier de l'Université de Montréal Research Centre Independent Ethics Committee. From 28 cases, 242 images from fluoroscopic spot films or DSA acquisitions were selected because they included either a PC and/or a DD.

2.3.1. Optimal parameters

The first 100 images were used to determine the optimal parameters for the numerical methods that achieved the best segmentation possible. Each image was revised by an expert who manually identified the different structures with line segments. The outlines of the DD were circumscribed in its 3 main parts: the pusher, the sheath (tubing including the folded SG), and the dilatator tip. The centrelines of the DD as well as other guidewires present were also traced with points to parameterize a cubic spline curve. Finally, the PC radiopaque marker centres were tagged. Since the identification process (ground truth) is quite obvious and no extreme precision is needed, only one expert processed the database, and only once.

The first task of this optimal inquiry was to establish the most efficient image-filtering method and its parameters. Using the SNR, and knowing the true locations of the object of interest, a mean score was attributed per method and per parameter. For the radiopaque marker of the PC, the Hessian filter and the GNS showed the best SNR score (Fig. 5). By revising the specific result of each method, it was observed that Hessian and GNS reacted differently on the same image, generating different false negatives and positives. The logical next step was then to use both methods in a hybrid operation to improve performances with regards to artefacts, improving segmentation that follows. The fusion of Hessian/GNS did indeed produce a better segmentation result and a mean SNR of 548.

The last task consisted of adjusting the optimal thresholds for the segmentation of structures. Again, using the ground truth, these thresholds were tuned to produce a sensitivity score equal to the positive predictive value. This means that the artefacts (false positives) are equivalent to the missed structures (false negatives). Fig. 6 illustrates the sensitivity and positive predictive value graph for the segmentation of the PC marker while testing different threshold parameters on all of the test images. The parameters were selected when the sensitivity and positive predictive values were both at 91%.

For the DD, a 3-pass Frangi filter was tuned to enhance the wide range of widths in pixel size, depending on the projection parameters (Fig. 7b). The threshold based on the Otsu ratio was then adjusted to 85% sensitivity and positive predictive value from the corresponding graph (Fig. 6).

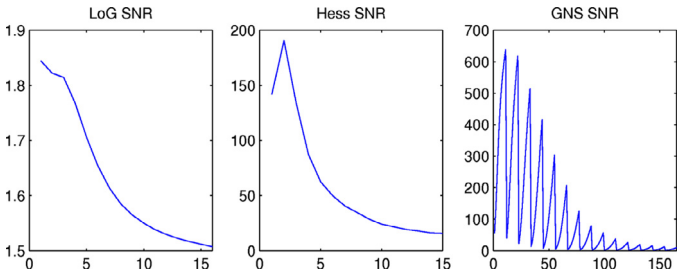

Fig. 5. Filtered SNR results (abscissa for LoG and Hessian is the gradient σ value, for the GNS, it is different set of σ and GNS iteration count).

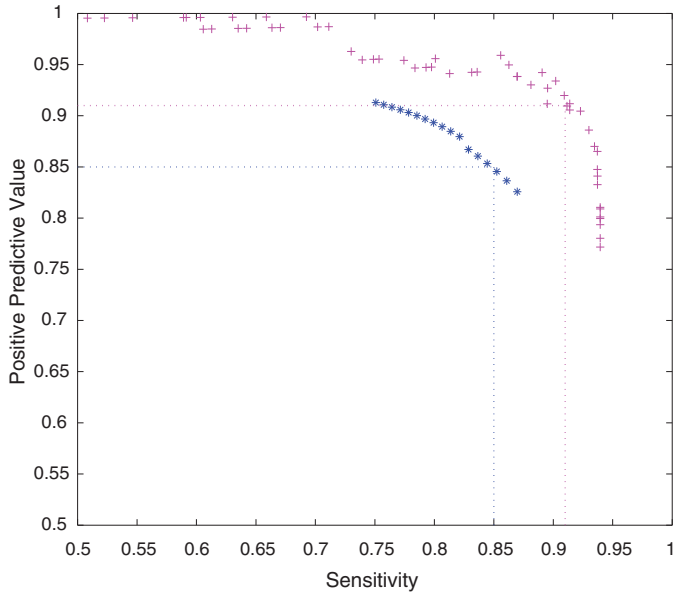

Fig. 6. Sensitivity versus positive predictive value of the selection of the radiopaque marker (blue $*$), and the delivery device thresholds (magenta (+)). (For interpretation of the references to color in this figure legend, the reader is referred to the web version of this article.)

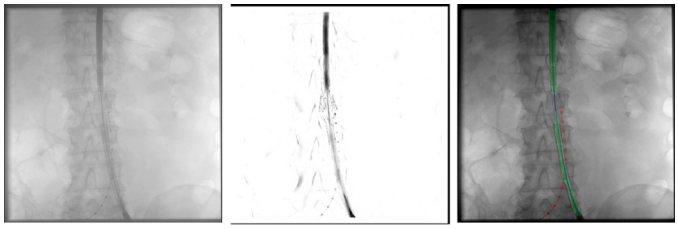

Fig. 7. Segmentation of delivery device (a) original image, (b) Frangi filter, (c) segmented device (green), localized radiopaque marker (red), and centreline (blue). (For interpretation of the references to color in this figure legend, the reader is referred to the web version of this article.)

Table 1
Endovascular devices automatic segmentation results.

	Sensitivity(%)	Positive predictive value(%)
Positive predictive value	85.9 ± 9.5	88.7 ± 14.8
DD sheath	63.4 ± 14.8	100
PC radiopaque marker	88.3 ± 21.9	96 ± 17.3

Note: DD=Delivery device; PC=Pigtail catheter

The optimally tuned numerical methods for the segmentation of the endovascular devices are summarized as follows:

Step 1. Pigtail catheter
- (a) Radiopaque enhancement filtering based on the fusion of Hessian and GNS filter
- (b) Segmentation threshold based on image size
- (c) Data analysis of patterns recognition base on
  - (i) marker distances within tolerance;
  - (ii) line segment orientation between markers within an acceptable curvature progression;
  - (iii) marker assembled in chain of 3 or more.

Step 2. Delivery device
- (a) Asymmetric vertical line enhancement filter based on Frangi
- (b) Segmentation threshold based on Otsu
- (c) Data analysis based on
  - (i) entry and exit points of the tool path in the image based on the pre-interventional centreline projections;
  - (ii) path tracking to seek new centrelines.

2.3.2. Validation

These newly proposed optimized algorithms were tested on the remaining 142 images. Using the ground truth produced by the expert manual identification, the automatic segmentation results were evaluated.

3. Results

Fig. 7 details an example of the enhancement and segmentation of the endovascular devices. From the original image 7 a, the DD is enhanced using the Frangi filter 7 b, the radiopaque markers are enhanced using the fusion Hessian/GNS filter, and all components are segmented using the calibrated threshold 7 c. The sensitivity and positive predictive values for all segmentation schemes are presented in Table 1.

3.1. Delivery device

The proportion of the area actually detected by the segmentation of the DD varied depending on its component. The pusher and dilatator tip are more radiopaque, therefore more visible on x-ray. They were detected at 85.9% occurrence. Most of the surfaces missed were near the edges and not along the length. The Frangi filter, combined with threshold segmentation, offered less precision on the edge detection because it is a filter, not an edge-tracking algorithm. The positive predictive value was 88.7%, slightly higher than in the training phase. The sheathed part of the DD enclosing the SG is less radiopaque, therefore more difficult to segment. Its surface was segmented at 63.4% occurrence, without artefacts (positive predictive value at 100%). It is the squeezed metallic struts of the SG inside the sheath that show more radiation absorption, but they are not continuous. In fluoroscopic images with a large field of view and larger pixel size, these struts are faint and difficult to differentiate from the background. In order to overcome the poor surface segmentation of the sheath component, the centreline extraction of this portion was tested. The centreline determined with the minimal path algorithm was compared with the centreline manually traced by the expert circumscribed in the sheath region. This latter test was evaluated by the mean distance between two lines in mm. This mean distance on the experimental image dataset was estimated at 0.74 mm (± 2.5 mm). Ultimately, since the DD outside diameter is constant, the mean diameter of the DD in the pusher component can be extrapolated along the device centreline when the extracted surface is smaller than this value.

3.2. Radiopaque pigtail catheter marker

The radiopaque markers were detected in 88.3% of cases (sensitivity) and the positive predictive value was estimated at 96%. Thus, artefacts (false positives) were less frequent than the missed markers (false negatives). All 9 false positive markers (artefacts) were located inside the vascular lumen. They were actually markers located on the SG itself. The small and unbalanced number of images with a PC (25 in the experimental dataset and 59 in the training dataset) can explain these differences between the training and the experimental dataset that was adjusted at 91%.

4. Discussion

The set of methods presented in this paper have been optimized to produce the best-expected outcome. It is difficult to judge if the resulting numbers are sufficient to achieve the ultimate goal of deformation of the vascular overlay and perform an elastic registration. The vascular lumen must be overlaid while inserting the DD to confirm the path of the endovascular navigation and to align the SG properly below the renal ostia before deployment. The renal arteries have approximately a 6 mm mean diameter; it was therefore considered that an error less than 3 mm would be fair for this type of intervention and 1 mm would be adequate. The centreline tracking error was estimated at a mean of 0.74 mm (± 2.5 mm), which appears sufficient for the final objective of elastic registration and deformation. The literature on segmentation of endovascular guidewires reports lateral errors in the range of 0.17–1.02 mm [15,16,18,19,22,23] when excluding false segmentation. Thus, the errors reported here are, without exception, consistent with comparative studies. No prior study has addressed the segmentation of the two interventional devices described in this paper. The fiducial markers detection largely studied in oncology have distinctive features driving tracking algorithms. But the PC marker has rotational symmetry compared to the distinguished reflectional symmetry of the oncology fiducial marker. Also, existing research on the segmentation of line-like endovascular devices addressed their centreline extraction rather than the full area that is needed as in the present study. Thus, the segmentation of PC marker and DD surface extraction could not be compared to the existing method. Future experiments are necessary to show whether a more precise estimation of DD width is required to reproduce contact points with the iliac or aortic wall, and to accurately calculate the vessel deformation. The PC marker localization occurrence of 88.3% was, however, sufficient since not all the markers were required in order to retrace the path of the catheter. Moreover, the workflow proposed here actually presented no artefact localized outside the vessel lumen. This is a major non-quantifiable improvement of fluoroscopic guidance.

5. Conclusion

This paper addressed the task of automatic segmentation of relevant endovascular devices used in AAA-EVAR intervention. It is a required milestone in the development of an automatic reshaping of the vascular structure overlaid on live images to correct the misregistration commonly observed after rigid 2D/3D registration. The

proposed method for the enhancement of the PC is a combination of Hessian filter and newly introduced gradient norm shift. After an optimized threshold operation, an analysis efficiently discriminated artefacts outside the lumen. The method for the enhancement of the DD was an asymmetric Frangi filter that favours mostly vertical structures. The optimized threshold was improved with a minimal path-tracing bottom to top using a priori knowledge of the vascular preoperative centrelines. A database of images taken during AAA-EVAR interventions was divided in two parts, first to calibrate the different parameters for the extraction of both devices, and then to extensively test the optimized algorithms. In the calibration phase, the original gradient norm shift filter presented here produced higher signal to noise ratio than popular blob-like structure enhancement techniques. It could be very efficient in future works on the tracking of fiducial marker used in oncology. In the second phase of experiment, the PC radiopaque markers were segmented with a sensitivity of 88.3% and a predictive positive value of 96%. The more visible part of the DD (the dilatator tip and pusher) were segmented with a sensitivity of 85.9% and a positive predictive value of 88.7%. The less visible part of the DD, i.e. the portion including the folded SG, was segmented with a sensitivity of 63.4%. This portion could be reconstructed using centreline extraction, with an accuracy of 0.74 mm, and an estimation of the sheath width determined by its diameter at the dilatator tip and pusher. The segmentation of endovascular tool surfaces instead of the sole centreline constitutes a novel tool detection. Although very promising, these segmentation strategies of endovascular devices during EVAR should be tested to enable landmarks for an automatic reshaping of the vascular structures. Also, the overall dependency on the accuracy of the 2D/3D registration generating the a priori data should be evaluated.

Conflict of interest

Marcus Pfister is an employee of Siemens AG, Healthcare Sector.

Funding

This work was supported by a joint grant from the Canadian Institute of Health Research and Siemens AG, Healthcare Sector (Forchheim, Germany) (CIHR-SME grant: ISO-93328 and IPR-124294).

Ethical approval

The data used in this article were acquired with the authorization of the Centre Hospitalier de l'Université de Montréal Research Centre Independent Ethics Committee (acceptance ID CE 09.058 and CE 12.333).

References

[1] Greenhalgh RM, Brown LC, Kwong GP, Powell JT, Thompson SG. Comparison of endovascular aneurysm repair with open repair in patients with abdominal aortic aneurysm (evar trial 1), 30-day operative mortality results: randomised controlled trial. Lancet 2004;364:843–8.
[2] Dardik A, Lin JW, Gordon TA, Williams GM, Perler BA. Results of elective abdominal aortic aneurysm repair in the 1990s: A population-based analysis of 2335 cases. J Vasc Surg 1999;30(6):985–95.
[3] Becquemin JP, Pillet JC, Lescalie F, Sapoval M, Goueffic Y, Lermusiaux P, et al. A randomized controlled trial of endovascular aneurysm repair versus open surgery for abdominal aortic aneurysm in low- to moderate-risk patients. J Vasc Surg 2011;53(5):1167–73.
[4] Brown LC, Brown EA, Greenhalgh RM, Powell JT, Thompson SG, on behalf of the UK EVAR Trial Participants. Renal function and abdominal aortic aneurysm (aaa): the impact of different management strategies on long-term renal function in the uk endovascular aneurysm repair (evar) trials. Annals of Surg 2010;251(5).
[5] Cross J, Gurusamy K, Gadhvi V, Simring D, Harris P, Ivancev K, et al. Fenestrated endovascular aneurysm repair. Br J Surg 2012;99(2):152–9.
[6] Carrell TWG, Modarai B, Brown JRI, Penney GP. Feasibility and limitations of an automated 2d-3d rigid image registration system for complex endovascular aortic procedures. J Endovasc Ther 2010;17(4):527–33.
[7] Dijkstra ML, Eagleton MJ, Greenberg RK, Mastracci T, Hernandez A. Intraoperative c-arm cone-beam computed tomography in fenestrated/branched aortic endografting. J Vasc Surg 2011;53(3):583–90.
[8] Kaladji A, Lucas A, Cardon A, Haigron P. Computer-aided surgery: concepts and applications in vascular surgery. Perspect Vasc Surg 2012;24(1).
[9] Kauffmann C, Tang A, Dugas A, Therasse E, Olivia V, Soulez G. Clinical validation of a software for quantitative follow-up of abdominal aortic aneurysm maximal diameter and growth by ct angiography. Eur J Radiol 2011;77(3):502–8.
[10] Fukuda T, Matsuda H, Doi S, Sugiyama M, Morita Y, Yamada M, et al. Evaluation of automated 2d-3d image overlay system utilizing subtraction of bone marrow image for evar: feasibility study. Eur J Vasc Endovasc Surg 2013;46(1):75–81.
[11] Penney G, Varnavas A, Dastur N, Carrell T. An image-guided surgery system to aid endovascular treatment of complex aortic aneurysms: description and initial clinical experience. In: Lecture Notes in Computer Sciences, 6689. Information Processing in Computer Assisted Interventions; 2011.
[12] Kaladji A, Dumenil A, Castro M, Cardon A, Becquemin J-P, Bou-Saïd B, et al. Prediction of deformations during endovascular aortic aneurysm repair using finite element simulation. Comput Med Imaging and Gr 2013;37:142–9.
[13] Kauffmann C, Douane F, Therasse E, Lessard S, Elkouri S, Gilbert P, et al. Source of errors and accuracy of two-dimensional/three- dimentional fusion roadmap for endovascular aneurysm repair of abdominal aortic aneurysm. J Vasc Interv Radiol 2015;4(26):544–51.
[14] Pauly O, Heibel H, Navab N. A machine learning approach for deformable guidewire tracking in fluoroscopic sequences. Med Image Comput Comput Assist Interv 2010;13:343–50.
[15] Baert SAM, van de Kraats EB, van Walsum T, Viergever MA, Niessen WJ. Three-dimensional guide-wire reconstruction from biplane image sequences for integrated display in 3-d vasculature. IEEE Trans Med Imaging 2003;22(10):1252–8.
[16] Barbu A, Athitsos V, Georgescu B, Boehm S, Durlak P, Comaniciu D. Hierarchical learning of curves application to guidewire localization in fluoroscopy. IEEE Comput Vis Pattern Recognit 2007:1–8.
[17] Bismuth V, Vancamberg L, Gorges S. A comparison of line enhancement techniques - applications to guide-wire detection and respiratory motion tracking. In: SPIE, editor. Medical Imaging 2009: Image Processing, 7259; 2009.
[18] Lessard S, Lau C, Chav R, Soulez G, Roy D, de Guise JA. Guidewire tracking during endovascular neurosurgery. Med Eng Phys 2010;32(8):813–21.
[19] Mazouer P, Chen T, Zhu Y, Wang P, Durlak P, Thiran J-P, et al. User-constrained guidewire localization in fluoroscopy. In: SPIE, editor. Medical Imaging, 7259; 2009.
[20] Palti-Wasserman D, Bruckstein AM, Beyar RP. Identifying and tracking a guide wire in the coronary arteries during angioplasty from x-ray images. IEEE Trans Biomed Eng 1997;44(2):152–64.
[21] Slabaugh GG, Kong K, Unal GB, Fang T. Variational guidewire tracking using phase congruency. In: Ayache N, Ourselin S, Maeder AJ, editors. MICCAI (2). Lecture Notes in Computer Science, 4792. Springer; 2007. p. 612–19.
[22] Spiegel M, Pfister M, Hahn D, Daum V, Hornegger J, Struffert T, et al. Towards real-time guidewire detection and tracking in the field of neuroradiology. In: SPIE, editor. Medical Imaging, 7261; 2009.
[23] Wang P, Zhu Y, Zhang W, Chen T, Durlak P, Bill U, et al. Hierarchical guidewire tracking in fluoroscopic sequences. In: SPIE, editor. Medical Imaging, 7259; 2009.
[24] Zarkh M, Klaiman M. Guide wire navigation and therapeutic device localization for catheterization procedure. In: Computer Assisted Radiology and Surgery, 1281; 2005. p. 311–16.
[25] Bender H-J, Männer R, Poliwoda C, Roth S, Walz M. Reconstruction of 3d catheter paths from 2d x-ray projections. Lecture Notes in Computer Science 1999;1679:981–9.
[26] Franken E, van Almsick M, Rongen P, Florack L, ter Haar Romeny BM. An efficient method for tensor voting using steerable filters. In: Leonardis A, Bischof H, Pinz A, editors. ECCV (4). Lecture Notes in Computer Science, 3954. Springer; 2006. p. 228–40.
[27] Meyer SA, Wolf PD. Registration of three-dimensional cardiac catheter models to single-plane fluoroscopic images. IEEE Trans Biomed Eng 1999;46(12):1471–9.
[28] Molina C, Prause G, Radeva P, Sonka M. 3-d catheter path reconstruction from biplane angiograms. SPIE 2007.
[29] Heibel H, Glocker B, Groher M, Pfister M, Navab N. Interventional tool tracking using discrete optimization. IEEE Trans Med Imaging 2013;32(3):544–55.
[30] Bismuth V, Vaillant R, Funck F, Guillard N, Najman L. A comprehensive study of stent visualization enhancement in x-ray images by image processing means. Med Image Anal 2011;15(4):565–76.
[31] Chen T, Wang Y, Durlak P, Comaniciu D. Real time assistance for stent positioning and assessment by self-initialized tracking.. Med Image Comput Assist Interv 2012;15(1):405–13.
[32] Demirci S, Bigdelou A, Wang L, Wachinger C, Baust M, Tibrewal R, et al. 3d stent recovery from one x-ray projection. Med Image Comput Assist Interv 2011;14(1):178–85.
[33] Ali I, Alsbou N, Herman T, Ahmad S. An algorithm to extract three-dimensional motion by marker tracking in the kv projections from an on-board imager: four-dimensional cone-beam ct and tumor tracking implications. J Appl Clin Med Phys 2011;12(2):223–38.
[34] Harris EJ, McNair HA, Evans PM. Feasibility of fully automated detection of fiducial markers implanted into the prostate using electronic portal imaging: A comparison of methods. Int J Radiat Oncology Biol Phys 2006;66(4):1263–70.
[35] Mao W, Riaz N, Lee L, Wiersma R, Xing L. A fiducial detection algorithm for real-time image guided IMRT based on simultaneous MV and kV imaging. Medical Physics 2008;35(8):3554–64.

[36] Nederveen A, van der Heide U, Dehnad H, van Moorselaar R, Hofman P, Lagendijk J. Measurements and clinical consequences of prostate motion during a radiotherapy fraction. Int J Radiat Oncology Biol Phys 2002;53(1):206–14.
[37] Tang X, Sharp GC, Jiang SB. Fluoroscopic tracking of multiple implanted fiducial markers using multiple object tracking. Phys Med Biol 2007;52(14):4081–98.
[38] Yaniv Z. Localizing spherical fiducials in c-arm based cone-beam ct. Med Phys 2009;36(11):4957–66.
[39] Schreibmann E, Xing L. Image registration with auto-mapped control volumes. Med Phys 2006;33(4):1165–79.
[40] Lindeberg T. Feature detection with automatic scale selection. Int J Comput Vis 1998;30(2):79–116.
[41] Liu J, White J, Summers R. Automated detection of blob structures by hessian analysis and object scale. In: Proceedings of IEEE International Conference on Image Processing; 2010. p. 841–4.
[42] Xu C, Prince J. Snakes, shapes, and gradient vector flow. IEEE Trans Image Process 1998;7(3):359–69.
[43] Frangi AF, Niessen WJ, Vincken KL, Viergever MA. Multiscale vessel enhancement filtering. In: Medical Image Computing and Computer-Assisted Intervention. In: Lecture Notes in Computer Science, 1496; 1998. p. 130–7.
[44] Otsu N. A threshold selection method from gray-level histograms. In: Proceedings of IEEE Transaction on Systems, Man and Cybernetics, 9; 1979.